

## THE MASS-SIZE RELATION FROM CLOUDS TO CORES. II. SOLAR NEIGHBORHOOD CLOUDS

J. KAUFFMANN<sup>1,2,\*</sup>, T. PILLAI<sup>2,\*</sup>, R. SHETTY<sup>1,2,\*</sup>, P. C. MYERS<sup>2</sup>, & A. A. GOODMAN<sup>1,2</sup>

*Draft version April 9, 2010*

### ABSTRACT

We measure the mass and size of cloud fragments in several molecular clouds continuously over a wide range of spatial scales ( $0.05 \lesssim r/\text{pc} \lesssim 3$ ). Based on the recently developed “dendrogram-technique”, this characterizes dense cores as well as the enveloping clouds. “Larson’s 3<sup>rd</sup> Law” of constant column density,  $m(r) \propto r^2$ , is not well suited to describe the derived mass-size data. Solar neighborhood clouds not forming massive stars ( $\lesssim 10 M_{\odot}$ ; Pipe Nebula, Taurus, Perseus, and Ophiuchus) obey

$$m(r) \leq 870 M_{\odot} (r/\text{pc})^{1.33}.$$

In contrast to this, clouds forming massive stars (Orion A, G10.15–0.34, G11.11–0.12) do exceed the aforementioned relation. Thus, this limiting mass-size relation may approximate a threshold for the formation of massive stars. Across all clouds, cluster-forming cloud fragments are found to be—at given radius—more massive than fragments devoid of clusters. The cluster-bearing fragments are found to roughly obey a mass-size law  $m \propto r^{1.27}$  (where the exponent is highly uncertain in any given cloud, but is certainly smaller than 1.5).

*Subject headings:* ISM: clouds; methods: data analysis; stars: formation

### 1. INTRODUCTION

Most of our present understanding of star formation processes is based on detailed studies of solar neighborhood molecular clouds (closer  $\sim 500$  pc). To this end past research has, e.g., studied the masses and sizes of dense cores in molecular clouds ( $\lesssim 0.1$  pc size) such as Perseus, Taurus, Ophiuchus, Orion, and the Pipe Nebula (e.g. Motte et al. 1998, Johnstone et al. 2000, Hatchell et al. 2005, Enoch et al. 2007). Further research studied clumps in these clouds (some 0.1 pc) and the clouds ( $\gtrsim 10$  pc) containing the cores (e.g., Williams et al. 1994, Cambr esy 1999, Kirk et al. 2006; see Williams et al. 2000 for definitions of cores, clumps, and clouds). This research does, however, not probe the relation between the properties of cores, clumps, and clouds: traditionally, every domain is characterized and analyzed separately. As a result, even in the solar neighborhood, it is still not known how the core densities (and thus star-formation properties) relate to the state of the surrounding cloud.

To be precise, we do in principle know a bit about the relation between cloud structure at large and small scale. For structure within molecular clouds, Larson (1981) concluded (in his Eq. 5) that the mass contained within the radius  $r$  obeys a power-law,

$$m(r) = 460 M_{\odot} (r/\text{pc})^{1.9}. \quad (1)$$

Most subsequent work refers to this relation as “Larson’s 3<sup>rd</sup> law”, and replaces the original result with  $m(r) \propto r^2$  (e.g., McKee & Ostriker 2007). This “law of constant column density” (with respect to scale,  $r$ ) is now considered one of the fundamental properties of molecular cloud structure (e.g., Ballesteros-Paredes et al. 2007, McKee & Ostriker 2007, Bergin & Tafalla 2007). We do, however, not know whether this relation is still consistent with up-to-date column density maps of molecular clouds.

Part I of the present series (Kauffmann et al. 2010) describes a new technique to extract mass-size relations from cloud maps. It is based on “dendrograms”, a tree-based segmentation of cloud structure (Rosolowsky et al. 2008). Here, we employ this technique to study the molecular clouds in Perseus, Taurus, Ophiuchus, Orion, and the Pipe Nebula. To illustrate the properties of more massive clouds, we also include data for two more distant clouds of high density (farther than 2 kpc; G10.15–0.34 and G11.11–0.12).

The present paper summarizes the analysis method in Sec. 2. The main quantitative analysis of the maps is presented in Sec. 3. Section 4 systematizes the results and interprets them in the context of our present knowledge of star formation regions. This discussion is supported by model calculations in Appendices A and B. We conclude with a summary in Sec. 5.

### 2. METHOD & DATA

#### 2.1. Data Processing

##### 2.1.1. Basic Map Analysis

Our basic analysis approach is summarized in Sec. 2.1 of part I, and illustrated in Fig. 1 of the same paper. In essence, starting from a set of local maxima, we contour a given column density map at all levels possible. For every contour, we derive the enclosed mass and area, A.

jens.kauffmann@jpl.nasa.gov

<sup>1</sup> Initiative in Innovative Computing (IIC), 60 Oxford Street, Cambridge, MA 02138, USA

<sup>2</sup> Harvard-Smithsonian Center for Astrophysics, 60 Garden Street, Cambridge, MA 02138, USA

\* present addresses: Jens Kauffmann, NPP Fellow, Jet Propulsion Laboratory, 4800 Oak Grove Drive, Pasadena, CA 91109, USA; Thushara Pillai, CARMA Fellow, Caltech Astronomy Department, 1200 East California Blvd., Pasadena, CA 91125, USA; Rahul Shetty, Zentrum f ur Astronomie der Universit at Heidelberg, Institut f ur Theoretische Astrophysik, Albert-Ueberle-Str. 2, D-69120 Heidelberg, Germany

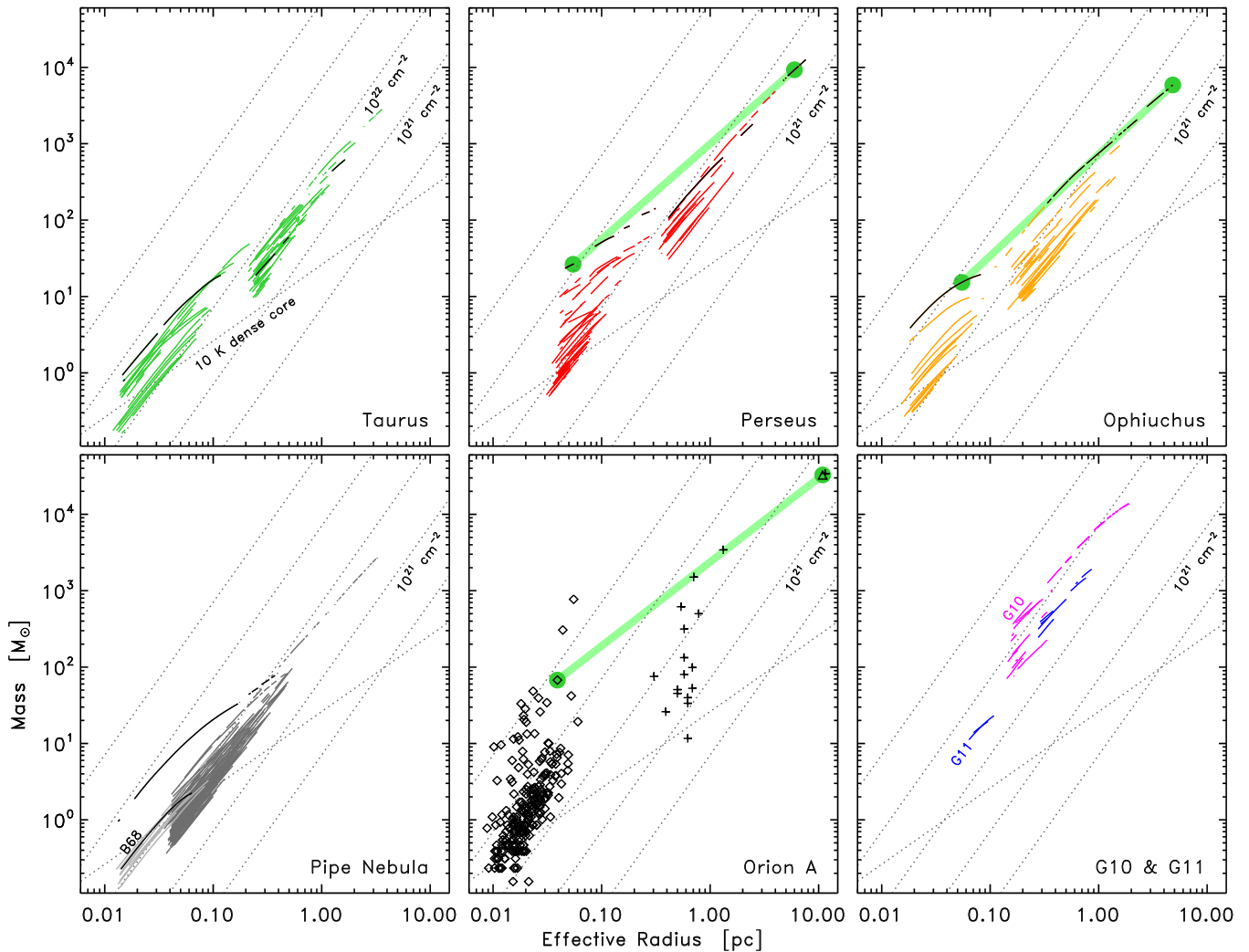


FIG. 1.— Mass-size relations for the clouds listed in Table 1. In most clouds, data from two different observational techniques (e.g., dust extinction and emission) are combined to provide a comprehensive picture probing a wide range of spatial scales. *Solid black lines* highlight cloud regions containing the most massive cloud fragment found for small radii. *Green lines starting in circles* indicate the global mass-size relations discussed in Section 2.1.2. The other *dotted lines* give reference mass-size relations as discussed in Sec. 2.1.3. In Orion A, published data extracted using CLUMPFIND-like approaches are plotted (*diamonds* mark SCUBA data, *crosses* indicate CO observations) instead of using the contour-based scheme employed here. Further, the *triangle* indicates the large-scale Orion A extinction mass measurement discussed in the text.

Following the terminology of Peretto & Fuller (2009), we define “cloud fragments” in the maps as such regions enclosed by a continuous column density contour. The area is used to derive effective radii,

$$r = (A/\pi)^{1/2}. \quad (2)$$

Subsequent contours are usually nested in the map. This defines a relation between measurements. This essentially yields series of mass-size measurements. In the plots shown in this paper, such series are drawn using continuous lines (e.g., Fig. 1).

In practice, the processing is implemented using the dendrogram map analysis technique introduced by Rosolowsky et al. (2008). As a bonus, this also yields diagnostic diagrams on the cloud hierarchy. We do not use this feature in the present paper, though.

In our analysis, we reject all cloud fragments that have a diameter (i.e.,  $2r$ ) smaller than the map resolution. Further, we require a minimum contrast between the lo-

cal maxima used to seed the contouring. Here, this limit is set to the noise level times a factor 3. Further, we do not characterize column densities below a certain threshold. As discussed below, Table 1 lists these parameters for each map studied here.

### 2.1.2. Calculation of Mass-Size Slopes

Part I demonstrates that mass-size data can conveniently be characterized using power-laws of the form

$$m(r) = m_0 (r/\text{pc})^b. \quad (3)$$

These are characterized by slope,  $b$ , and intercept,  $m_0$ . As shown in part I, slopes can be derived using various methods. As demonstrated in part I,  $b \leq 2$  in our work, since  $b > 2$  would imply an increase of the mean column density with radius.

We define global slopes to capture trends between small and large spatial scales (Sec. 4.3 in part I). To calculate these, we derive the maximum fragment masses,

$m_{\max}$ , observed at radii of  $r_{\text{sm}} = 0.05$  pc and  $r_{\text{lg}} = 5.0$  pc. (These radii are chosen to permit comparison between clouds, as becomes more obvious below.) Based on these, we derive the global slope,

$$b_{\text{glob}} = \frac{\ln[m_{\max}(r_{\text{lg}})/m_{\max}(r_{\text{sm}})]}{\ln[r_{\text{lg}}/r_{\text{sm}}]}. \quad (4)$$

As illustrated in Fig. 1, this slope is defined such that  $m(r) \propto r^{b_{\text{glob}}}$  connects the mass and size measurements at 0.05 pc and 5.0 pc radius (for appropriate intercept).

To characterize trends at a given spatial scale, we use tangential slopes (Sec. 4.4 in part I). These are derived infinitesimally at a given radius,

$$b(r) = \left. \frac{d \ln(m[r'])}{d \ln(r')} \right|_{r'=r}. \quad (5)$$

As illustrated in Fig. 7 of part I, the measured slopes are smoothed and filtered to improve the data quality.

### 2.1.3. Reference Mass-Size Relations

Section 3.1 of part I introduces various reference mass-size relations. These can be used to navigate more intuitively within the data space. They are thus featured in most figures of the present paper (e.g., Fig. 1). Specifically, lines of constant mean column density obey a mass-size law  $m(r) \propto r^2$ . Our plots contain relations for mean column densities separated by factors of 10. Static equilibrium models of isothermal spheres, on the other hand, obey  $m(r) \propto r$ . We draw a model relation for a gas temperature of 10 K.

We stress that we obtain two-dimensional mass-size relations from column density maps. These are related to, but not identical with, mass-size laws obtained from three-dimensional density maps. This is further explored in Sec. 4.3.

## 2.2. Combining Data for several Clouds

Part I describes in detail how dust extinction and emission maps can be used to derive column density maps for molecular cloud complexes. Once calibrated to a common mass conversion scale (Sec. 4.2 of part I), dust extinction and emission data for a given cloud can be combined to probe the masses and sizes across a vast range of spatial scales. In part I, we did this for Perseus only. Here, we combine our Perseus data with maps of other clouds. We do this by repeating the analysis already carried out for Perseus.

We start with a survey of a sample of well-studied nearby clouds that are essentially devoid of high-mass stars. Besides the Perseus molecular cloud, those in Taurus, Ophiuchus, and the Pipe Nebula are examined here. As a general reference to clouds also forming high-mass stars, we include the Orion A cloud. Then, the more remote G10.15–0.34 (hereafter G10;  $\sim 2.1$  kpc) and G11.11–0.12 complexes (hereafter G11;  $\sim 3.6$  kpc) are studied to build a first bridge towards the study of relatively distant sites of high mass star formation (see Pillai et al. (2007) for distances and references; G10 is further discussed by Wood & Churchwell (1989) and Thompson et al. 2006, while Pillai et al. (2006b) study G11). Note that G11 is an Infrared Dark Cloud (IRDC; see Menten et al. 2005 and Beuther et al. 2007 for reviews).

A data summary for our sample is provided in Table 1. This includes parameters used for the source extraction.

### 2.2.1. Data and Analysis

The extinction map analysis for Ophiuchus (Ridge et al. 2006) and the Pipe Nebula (Lombardi et al. 2006) is analogous to the one for the Perseus cloud carried out in part I. The visual extinction in the Pipe Nebula map is reduced by 1.34 mag (reduction of 0.15 mag in  $A_K$ ), following the analysis by Lombardi et al. (2008). For Taurus, we use the map by Rowles & Froebrich (2009). Its resolution varies throughout the map. This is analogous to a region-dependent smoothing, which may affect mass estimates (Sec. 4.1 in part I). We thus use this map with caution. In Taurus (Kauffmann et al. 2008) and Ophiuchus (Enoch et al. 2007) the processing of the dust emission maps follows the Perseus Bolocam analysis of part I. *Note that the Taurus MAMBO maps do not cover all of the cloud and may therefore give a biased view of the dense core conditions.* Pipe Nebula regions with high column density must be probed in detail. To do this, we include a SCUBA map for B68 (Alves et al. 2001), which is kindly provided by J. Alves. Román-Zúñiga et al. (2009) mapped the Pipe’s B59 region in extinction. We process these maps using our analysis scheme. For all sources, Table 1 lists the free parameters used in our source extraction algorithm.

The resulting mass-size relations form part of Fig. 1. To illustrate some aspects of the spatial cloud structure, Fig. 1 highlights (in black) for every cloud the mass-size evolution of the most massive fragment found at small radii. Note that, in Taurus and the Pipe Nebula, these fragments do *not* form part of the largest cloud fragments found in the maps.

In Orion A, no data suited for a reliable dendrogram structure analysis of column densities is yet available. Instead, we use the Rowles & Froebrich (2009) extinction maps to derive a single mass and size measurement on the largest scales probed by that map. On smaller scales, the extinction map is not reliable because of too few background sources. For reference, we also plot mass and size measurements for  $^{13}\text{CO}$  clumps in Orion, as published elsewhere (Bally et al. 1987; their Table 1, plus text statements). These data are, however, not used in the quantitative analysis. At smaller scales, we fold in published data from SCUBA studies employing CLUMPFIND-like data analysis methods (Nutter & Ward-Thompson 2007). As illustrated in Fig. 4 of part I, at given radius, these set a lower limit to the maximum dendrogram-derived masses usually employed here.

For G10 (the data are kindly provided—in advance of publication—by M. Thompson, J. Hatchell, and F. Wyrowski) and G11 (Carey et al. 2000), we run our contour analysis on SCUBA maps to derive mass-size data on large spatial scales. In G11, the structure on very small scales is probed in a similar fashion, using interferometric dust emission maps obtained using the Submillimeter Array (SMA; Pillai et al., in prep.). Unfortunately, the SMA map does not cover all of G11, and the derived mass-size data are likely to be biased (i.e., the most dense core is not covered by our data). We do not use our existing SMA data for G10, since the data is

TABLE 1  
DATA INCLUDED IN THIS STUDY.

Region / Distance	Data	Resolution	Noise mag	Rejection Threshold mag	Reference
<i>clouds only forming low-mass stars:</i>					
Taurus $d = 140$ pc	extinction dust emission (10.0 K)	$\leq 6'$ $20''$	0.4 1.4	2.0 4.3	Rowles & Froebrich (2009) Kauffmann et al. (2008)
Perseus $d = 260$ pc	extinction dust emission (12.5 K)	$5'$ $30''$	0.4 1.4	2.0 4.3	Ridge et al. (2006) Enoch et al. (2006)
Ophiuchus $d = 120$ pc	extinction dust emission (12.5 K)	$5'$ $30''$	0.6 2.5	2.0 7.6	Ridge et al. (2006) Enoch et al. (2007)
Pipe Nebula $d = 130$ pc	extinction	$60''$	0.5	4.0	Lombardi et al. (2006)
B59 $d = 130$ pc	extinction	$20''$	1.2	3.6	Román-Zúñiga et al. (2009)
B68 $d = 130$ pc	dust emission (10.0 K)	$15''$	1.1	3.3	J. Alves, priv. comm.
<i>clouds also forming high-mass stars:</i>					
Orion A $d = 414$ pc	$^{13}\text{CO}$ dust emission (20.0 K)	$1'7$ $14''$	— —	— —	Bally et al. (1987) Nutter & Ward-Thompson (2007)
G10.15–0.34 $d = 2100$ pc	dust emission (20.0 K)	$14''$	6.4	19.2	Thompson et al., in prep.
G11.11–0.12 $d = 3600$ pc	dust emission (15.0 K) dust emission (15.0 K)	$14''$ $4''$	6.6 4.9	19.7 14.6	Carey et al. (2000) Pillai et al., in prep.

misleading in this context (our G10 map only covers a minor dust emission peak). In the SCUBA and SMA maps, structure larger than a certain spatial scale is removed during data reduction. Setting other uncertainties aside, the true intensities and column densities will therefore be larger than derived here. The adopted dust temperatures are inspired by Pillai et al. (2006a) and Pillai et al. (2007).

### 2.2.2. Mass Estimates

Table 1 lists (as part of the data column) the dust temperatures adopted for each cloud. The temperatures for individual fragments may deviate from these mean values by several Kelvin. This introduces an associated uncertainty in mass estimates from dust emission. An uncertainty of order 25% is probably reasonable for extreme cases.

For Taurus, Figure 1 reveals a jump of order of a factor 2 in the mass-size relation from dust extinction to dust emission data, with the dust emission data implying the higher masses. This suggests a problem in the relative calibration of tracers, or a problem with the generation of the extinction map<sup>4</sup> Here, we use the Taurus extinction map with caution in our analysis.

B59 of the Pipe Nebula map appears to suffer from even larger mass biases; for exactly the same region, when compared to the Román-Zúñiga et al. (2009) results, the lower-resolution Lombardi et al. (2006) map

<sup>4</sup> The other extinction maps used here—created by Lada, Alves, Lombardi, and collaborators—use a spatially constant resolution. Also, the calculation of the extinction for a given star differs in details.

implies masses lower by a factor  $\sim 3$ . Given the extreme column densities in the target region (B59), this result is not entirely surprising. We do not expect such biases in the other regions (where areas of high column density are anyway probed by dust emission). Still, the B59 results suggest to use extinction maps with extreme caution.

## 3. MASS-SIZE RELATIONS: A CLOUD SAMPLE

At this point, all mass-size data has been collected and processed. In the following sections, we highlight three particular trends seen in this sample data.

In principle, the mass-size data for a given cloud might significantly depend on the viewing direction. Since we can only observe the cloud projections as seen from earth, our data might be biased because of our specific viewing direction. Here, we make the assumption that this is not the case. This notion is supported by our observational findings: all nearby clouds not forming massive stars have (in a broad sense) similar properties. Also, mass-size differences between clouds correlate with projection-independent cloud properties (e.g., for given radius, clouds forming massive stars are more massive). This suggests that projection effects do not significantly bias the mass-size laws derived here.

### 3.1. A limiting Mass-Size Relation for Massive Star Formation?

As a first characterization of the cloud sample, we look at the maximum radius-dependent mass of cloud fragments. We begin with clouds not forming massive stars. In the  $0.01 \lesssim r/\text{pc} \lesssim 10$  radius range, essentially all fragments in such clouds have a mass smaller than some

limiting law,

$$m(r) = 870 M_{\odot} (r/\text{pc})^{1.33}. \quad (6)$$

Figure 2 gives an illustration. This limit thus gives the typical mass range for structure in clouds like Taurus, Perseus, Ophiuchus, and the Pipe Nebula.

In detail, this relation excludes a bright fragment in NGC1333, which we remove from our analysis as a possibly unphysical outlier (its estimated mass exceeds those of other fragments of similar size by a factor 2, possibly because of neglected protostellar heating). The limiting law is derived by searching for the smallest intercept for which  $m_0 (r/\text{pc})^b$  does still provide an upper limit to the data. Practically, this is done by varying  $b$  until  $\max[m(r)/(r/\text{pc})^b]$  is minimized.

Interestingly, our sample clouds with massive star formation exceed the limiting relation (Eq. 6). This is shown in Fig. 2(b). For the Orion A cloud and G10, we derive an excess of up to a factor 10 in the  $0.01 \lesssim r/\text{pc} \lesssim 2$  radius range. This suggests that these clouds have a structure significantly different from what is found for clouds not containing such stars (Fig. 2[a]). In this light, Eq. (6) may approximate a limit for massive star formation: it could be that only clouds also containing fragments that exceed Eq. (6) are able to form massive stars. Larger samples of clouds forming massive stars must be screened to prove this point. Note, however, that most fragments in Orion A do fulfill Eq. (6). This cloud does therefore also contain objects that have masses and sizes not distinguishable from those found for clouds not forming massive stars.

As a mass-size limit for clouds not forming massive stars, Eq. (6) is probably uncertain to just a few 10%. If we, e.g., not use Ophiuchus data in the derivation of Eq. (6), then Ophiuchus would exceed the resulting mass-size limit by 30%. If we do the same with Perseus data, the excess is 15%. It is plausible to expect similar changes for other regions not forming massive stars. Observational uncertainties are most likely of a similar order, if one adopts the mass measurement techniques used here (i.e., dust emission and extinction). Then, several uncertainties (e.g., dust opacities) are simply removed by calibration to the same standard. In an absolute sense (i.e., when considering the true masses), Eq. (6) is as accurate as the mass conversion standards used here (e.g., relation of dust emission and mass). These are probably uncertain to less than a factor 2.

We stress that, excluding observational uncertainties, Eq. (6) provides a strict upper mass limit to the solar neighborhood sample *as we have defined it here*. Clouds violating Eq. (6) are not similar to the clouds in the solar neighborhood sample discussed here. This statement is sufficient for many purposes.

### 3.2. Local Clouds obey similar Mass-Size Relations at large Scales

Inspection of Figs. 1 and 2 suggests that all solar neighborhood clouds have similar masses at given size for radii  $\gtrsim 1$  pc. Specifically, the most massive fragments at given radius are essentially all within  $\pm 30\%$  of

$$m(r) = 400 M_{\odot} (r/\text{pc})^{1.7} \quad (7)$$

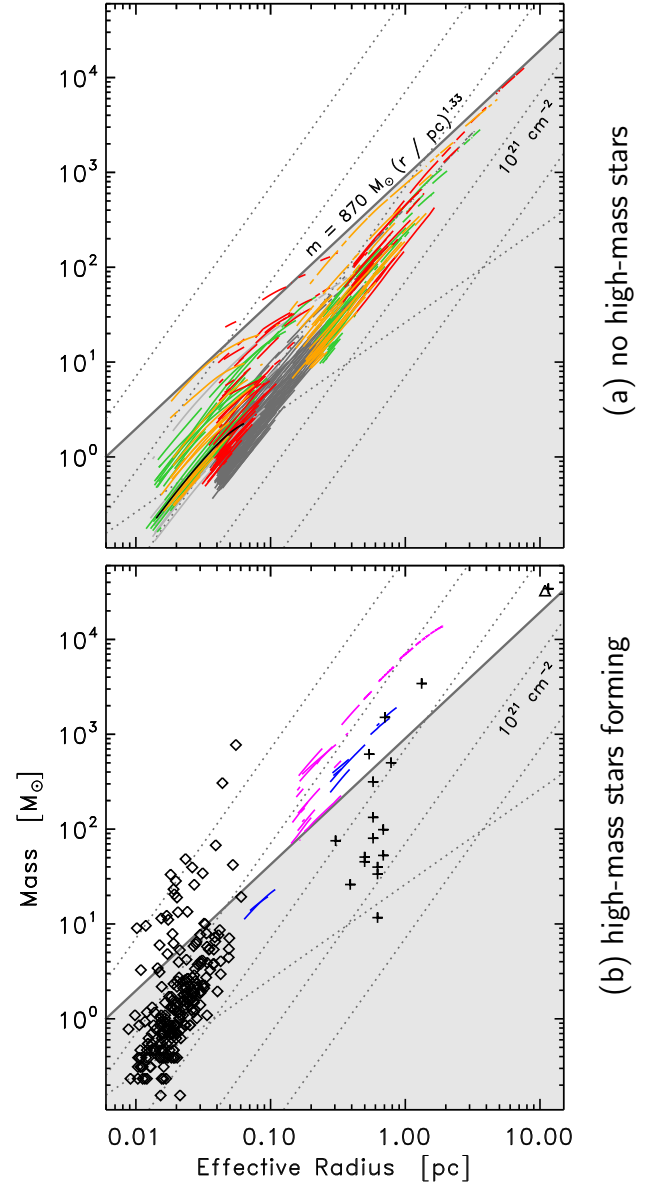


FIG. 2.— Joint mass-size plot for all clouds, separated into clouds with (*bottom*) and without (*top*) active formation of high-mass stars. See Fig. 1 for color coding. The *shading* indicates the approximate mass limit for fragments in clouds without high-mass star formation (*top panel*; Eq. 6). In our sample, all clouds forming high-mass stars contain fragments that exceed this limit (*bottom*). See Sec. 3.1 for details.

in the  $1 \leq r/\text{pc} \leq 4$  radius range, when considering Taurus, Ophiuchus, Perseus, and the Pipe Nebula. Also our preliminary Orion A data is, at 11 pc radius, within 40% of this law—with the caveat that we cannot examine whether Orion A follows Eq. (7) down to  $\sim 1$  pc radius. It thus appears that—with Orion A as a possible exception—all local clouds are similar in their large-scale mass structure.

This mass-size relation is very similar to the one originally derived by Larson (1981),  $m(r) = 460 M_{\odot} (r/\text{pc})^{1.9}$  (see Eq. 1 above). Our study thus confirms his result—but only for spatial scales  $\gtrsim 1$  pc. As we show throughout this paper (e.g., Eq. [6] and Figs. 4 and 5), no single mass-size relation describes all structural aspects of our

observational data.

Some cloud fragments  $\gtrsim 1$  pc are, however, much more massive than solar neighborhood clouds of similar size. G10, for example, violates Eq. (7) by about an order of magnitude. The similarity between local clouds implied by Eq. (7) might thus only hold for the solar neighborhood.

### 3.3. Clusters vs. Isolated Star Formation

It is obvious that the formation of a cluster requires a larger mass reservoir than necessary to form a single isolated star. Thus, one might naively expect that regions containing clusters are more massive than those devoid of stellar groups. If true, one would thus expect that, within a given cluster-forming cloud, the regions containing clusters are more massive than cluster-less regions of similar size. This hypothesis is tested in Sec. 3.3.1. Also, one would expect that cluster-forming cloud fragments are more massive than all similar-sized fragments in clouds not containing clusters. Section 3.3.2 investigates this issue.

In our sample, the Pipe Nebula and Taurus serve as examples of regions dominated by isolated star formation. Actually, except for B59, the Pipe Nebula does hardly form stars at all (Forbrich et al. 2009). Perseus and Ophiuchus serve as examples for cluster-forming regions. They do contain clusters much more significant than any stellar aggregate found in Taurus and the Pipe Nebula<sup>5</sup>. Orion A is another example of a cluster-forming cloud.

#### 3.3.1. Cluster-forming Fragments dominate their Host Cloud

We examine whether cluster-forming cloud fragments dominate the mass reservoir of their host cloud at all radii. This is executed in Fig. 1. Here, we only consider cluster-forming clouds with high quality data, i.e. Perseus and Ophiuchus. Inspection of the column density maps reveals that the (highlighted) most massive small-scale features in Perseus and Ophiuchus are located in the NGC1333 and L1688 clusters, respectively. At small spatial scales, the most massive fragments are thus indeed located in cluster-forming regions. Note, though, that cluster-forming regions do also contain fragments of lower mass. This is illustrated in the rightmost panel of Fig. 6 in part I: Bolocam-detected fragments in NGC1333 cover a wide range in mass.

In Ophiuchus, when examining larger spatial scales, fragments containing L1688 continue to be the most massive ones. This is not exactly true for NGC1333 in Perseus, though. In this cloud, when considering extinction maps, other fragments (drawn in red) are—by a small margin—the most massive ones at given radius. However, closer inspection (not presented here in detail)

<sup>5</sup> Clusters in nearby clouds were recently surveyed by Gutermuth et al. (2009). Based on Spitzer data, Ophiuchus and Perseus are found to contain clusters with  $\gtrsim 130$  members. The same study gives  $\sim 40$  members for L1495 in Taurus. This latter value is in line with previous studies and sets an upper limit to the size of stellar groups in Taurus (Table 4 of Kenyon et al. 2008). In the Pipe Nebula, the star formation activity is dominated by the B59 region (Forbrich et al. 2009). This group has  $\sim 20$  members (Brooke et al. 2007). Taurus and the Pipe Nebula do thus not contain clusters as significant as the ones in Perseus and Ophiuchus.

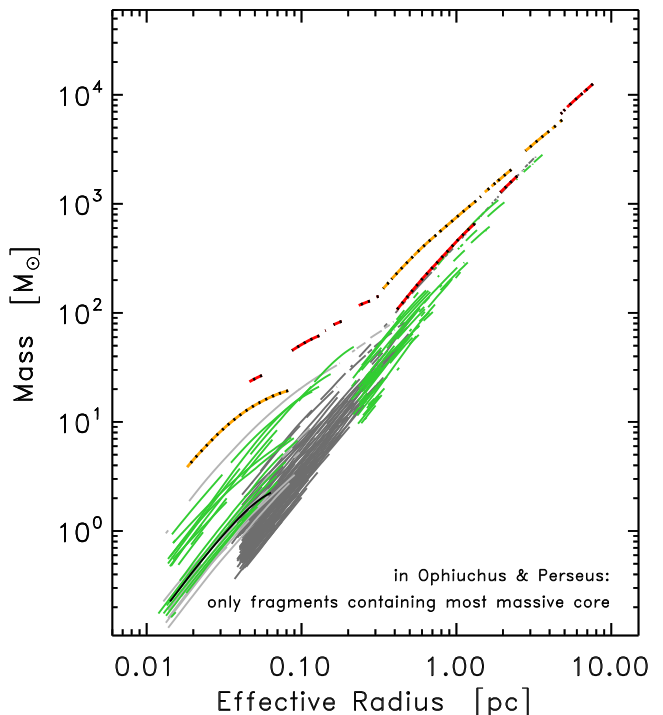


FIG. 3.— Perseus and Ophiuchus cloud regions containing the most massive cloud fragment found for small radii (highlighted by dotted black lines) in comparison to structure in Taurus and the Pipe Nebula. See Fig. 1 for color coding. Section 3.3 describes that cluster-forming fragments exceed, at given size, those without clusters in mass.

reveals that these fragments all contain the cluster IC348. In summary, cluster-forming fragments do thus indeed constitute the most massive cloud features at given radius. Some cluster-bearing fragment, which constitutes the most massive cloud fragment at some radius, might however at a different radius be less massive than some other cluster-forming fragment. In this context, note that IC348 is probably much older than NGC1333 (e.g., Gutermuth et al. 2009). Dense star-forming cores, which manifest as small objects of large mass, are thus actually not expected to remain in the IC348 region.

#### 3.3.2. Cluster-forming Fragments exceed Fragments without Clusters in Mass

Figure 3 compares cluster-forming cloud fragments to clouds devoid of significant clusters. For Taurus and the Pipe Nebula, the mass-size data is presented as done before (e.g., Fig. 1). We stress again that the Taurus MAMBO data for small spatial scales does not cover the entire cloud. At  $r \lesssim 0.2$  pc, the data only characterize the conditions in regions devoid of significant stellar groups. For Perseus and Ophiuchus, we choose a different plotting scheme. Here, we only plot the data for fragments containing the most massive fragment found at small radii (NGC1333 in Perseus, L1688 in Ophiuchus).

We find that, at given radius, cluster-forming Ophiuchus cloud fragments (i.e., towards L1688) are significantly more massive than those in Taurus and Pipe. The naive expectation (i.e., that cluster-forming fragments are more massive) is thus confirmed. For Perseus (i.e., towards NGC1333), however, the result is more nuanced. At  $r \lesssim 0.3$  pc, cluster-forming fragments are significantly

more massive than any structure in Taurus or the Pipe Nebula. For  $0.4 \lesssim r/\text{pc} \lesssim 2$ , however, the extinction-derived mass towards NGC1333 is similar to the maximum extinction-based masses for Taurus and the Pipe Nebula. If true, this would suggest that some cluster-forming regions at  $r \gtrsim 0.4$  pc have a structure similar to clouds only forming isolated stars (or no stars at all).

It may be, though, that the Perseus extinction-based masses are biased towards lower values. The Perseus map has relatively poor physical resolution ( $5'$  at 260 pc distance), and intrinsic colors of stars in NGC1333 can bias extinction measurements. These problems are amplified by high column densities towards NGC1333. Section 2.2.1 demonstrates these problems for B59. Thus we speculate that, at given size, the region containing NGC1333 is indeed more massive than any structure in Taurus and the Pipe Nebula. This remains to be proven, though.

The fragments in the Orion Nebula Cluster, as well as Orion A as an entire cloud are more massive than any feature in Taurus and the Pipe Nebula (Fig. 2). These data are thus consistent with the aforementioned trend.

In summary, fragments containing clusters appear to be more massive than all structure in clouds devoid of clusters. Larger samples, and better data, are needed to ultimately establish this trend.

### 3.4. Global Slopes of cluster-forming Regions

As we just have seen in Sec. 3.3.1, cluster-forming regions dominate the mass reservoir of their host cloud at any given spatial scale. This suggests a tight correlation between the properties of the cluster-forming fragments and the large-scale cloud structure. This can, for example, be characterized by “global” slopes of connection lines between mass-size measurements of the most massive fragments at large and small scale (Eq. 4). Since we lack comprehensive data on all spatial scales, we are unfortunately presently unable to derive global slopes for G10 and G11. To do so, one must also carefully characterize flux losses due to spatial filtering, as they occur in bolometer and interferometer maps. This is beyond the scope of the present paper.

Specifically, the cluster-forming clouds are probed both at  $\sim 0.05$  pc and  $\sim 5.0$  pc radius (e.g., Fig. 1). We calculate their global slopes by connecting the most massive fragments detected within 10% of these reference radii (30% radius deviation for the sparsely sampled Orion data). For Orion, where only very large scales are probed reliably, we use a mass measurement at 11 pc radius for slope calculations. Also, in Orion, the  $\gg 100 M_{\odot}$  fragments at  $\sim 0.05$  pc radius (right in the center of the Orion Nebula) are rejected as outliers. This rejection of objects is a regrettable move, since cloud fragments with extreme properties could be the actual sites where the most massive stars are born. However, we feel that a more detailed and careful analysis than possible here, including a detailed consideration of the temperature structure, is warranted. We hope to do this in one of our future studies. The resulting slopes range from 1.10 to 1.33, as shown in Fig. 4. Note that a much smaller slope (as small as  $\sim 0.7$ ) would hold for Orion A, if we do not reject the outliers. The uncertainties indicated in Fig. 4 hold for an uncertainty of a factor 2 in the mass ratio (factor 4 for the less reliable Orion data). This error budget presents

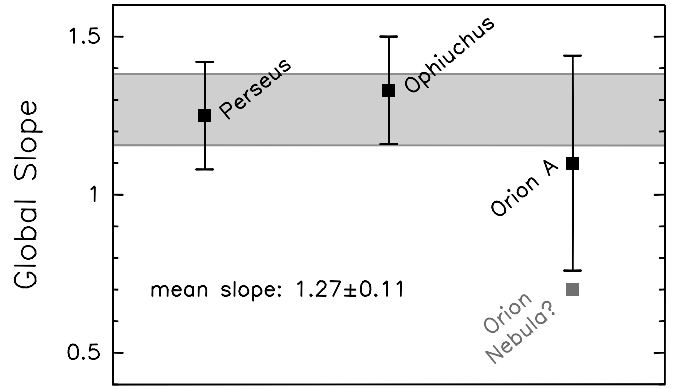


FIG. 4.— Global slopes for cluster-forming clouds. The slopes refer to the trends indicated in Fig. 1; the calculation of uncertainties is discussed in the text. The uncertainty-weighted mean slope of the sample is  $1.27 \pm 0.11$ . All clouds are consistent with having this slope, but the individual slope uncertainties are significant. If we include (highly uncertain) Orion Nebula data, slopes as low as  $\sim 0.7$  are found. See Sec. 3.4 for details.

the worst expected scenario; the true errors are probably smaller. In Ophiuchus, we have sufficient resolution to also measure masses at  $\sim 0.02$  pc radius. If we use such higher resolution data for this cloud, the slope decreases to 1.30.

Note that we experimented with different approaches to define global slopes to characterize the core-cloud structure. We then decided to use the current method using masses only at 0.05 pc and 5.0 pc because we find no significant differences compared with the other methods. For example, following the construction of Eq. (6), we measure for each cloud the slope,  $b$ , that minimizes  $\max[m(r)/(r/\text{pc})^b]$ . This value is then derived by utilizing data at all spatial scales. Slopes derived in this fashion only differ by  $\pm 0.04$  from those shown in Fig. 4, though. In the end, Eq. (4) appears to provide the simplest approach that can also be repeated by other researchers.

The uncertainty-weighted mean global slope for the three regions is  $1.27 \pm 0.11$ . As shown in Fig. 4, our data are consistent with the hypothesis that all cluster-forming clouds have the same global slope. This suggests that mass-size relations  $m \propto r^{1.27 \pm 0.11}$  provide a crude tool to use mass measurements at large spatial scale ( $\sim 5$  pc) to gauge the star formation conditions of the most massive embedded regions ( $\sim 0.05$  pc). Unfortunately, the extreme SCUBA cores in Orion A, with masses  $\gg 100 M_{\odot}$ , suggest that much smaller slopes may hold in some clouds. The data are incompatible with larger slopes, though. Thus, the uncertainties shown in Fig. 4 suggest that the slopes are not larger than 1.5.

### 3.5. Tangential Slopes: A Transition to Dense Cores?

Figure 5 presents tangential slopes for the entire sample. Because of too strong spatial filtering, we exclude maps taken with interferometers, SCUBA, and Bolocam from this calculation. For MAMBO, Taurus fragments larger  $r = 0.1$  pc might be affected by filtering (Kauffmann et al. 2008). Their slopes are thus not drawn.

A first trend noted in Fig. 5 is that the infinitesimal slopes change with radius. Also, they have no obvious relation to the global slopes shown in Fig. 4. Both slope

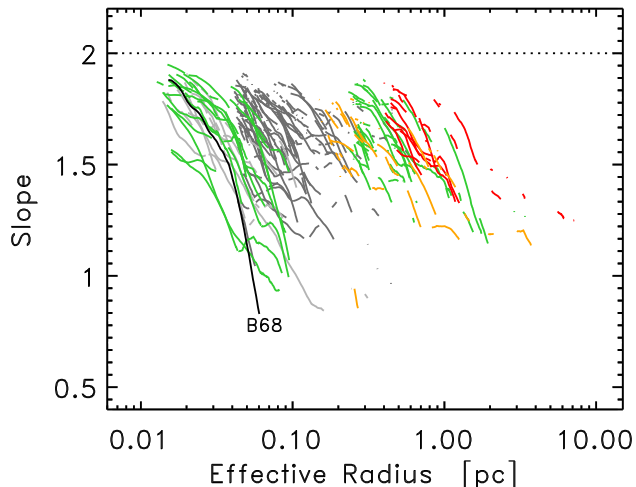


FIG. 5.— Tangential slopes for the sample clouds. See Fig. 1 for mark-up and coloring. The *dotted line* indicates the upper slope limit inherent to our measurement technique (Sec. 2.1.2). Because of spatial filtering, slopes from Taurus MAMBO data may be biased for  $r \gtrsim 0.1$  pc; such data are removed here. Data from other bolometers are not drawn because of the same problem. The *black line* gives the slope for B68, a Bonnor-Ebert-like dense core; similar slope trends are expected for other cores resembling Bonnor-Ebert spheres. See Sec. 3.5 for details.

definitions are thus complementary.

At given spatial scale  $\gtrsim 0.5$  pc (in this domain, we only have data for Perseus, Taurus, and Ophiuchus), all clouds have comparable infinitesimal slopes. Those for Ophiuchus are a bit lower than for the other regions, indicating that the observed clouds differ in their structure at  $r \gtrsim 0.5$  pc. In all clouds the slopes decrease with increasing radius. As we detail in Sec. 4.3, this behavior resembles the mass-size trends for model clouds with finite extent (i.e., density vanishes outside a finite radius).

In Taurus and the B59 and B68 regions of Ophiuchus, we derive very small infinitesimal slopes for  $r \lesssim 0.1$  pc. (These regions are the only ones well probed at such small scales.) Near  $r = 0.1$  pc, some fragments are observed to have slopes as low as  $d \ln(m)/d \ln(r) \sim 1$ . This result is not entirely unexpected. Spheres supported by isothermal pressure, for example, obey  $d \ln(m)/d \ln(r) = 1$  at intermediate radii (Sec. 4.3). Such (Bonnor-Ebert) spheres are commonly believed to constitute good idealizations of dense core structure. In particular, B68 is today quoted as the textbook model of a Bonnor-Ebert sphere (Alves et al. 2001). As expected, B68 shows a slope approaching 1 for large radii. We caution that the spatial filtering of bolometer maps, as well as the removal of extended features in extinction maps, might bias the slope measurements towards lower values. However, at least for cores with simple geometries, like B68, slopes  $\sim 1$  are expected for larger radii. This is required for Bonnor-Ebert-like density profiles. If such slopes were not observed, the paradigm of Bonnor-Ebert-like dense cores (e.g., Bergin & Tafalla 2007) would not be consistent with our data.

Note that the Taurus and Perseus infinitesimal slopes at  $r \sim 0.5$  pc are much larger than the slopes expected for the embedded dense cores of simple geometry ( $\sim 1$  for every core at some radius). If this dichotomy is real, it has interesting implications. Basically, the slope must

decrease from  $\gtrsim 1.5$  at  $r \gtrsim 0.5$  pc to  $d \ln(m)/d \ln(r) \sim 1$  for radii  $\lesssim 0.1$  pc. In other terms, there appears to be a transition in slope from the diffuse cloud structure to self-gravitating dense cores, when considering decreasing radii. Again we must caution that these trends might partially reflect artifacts in the data. As demonstrated before (Sec. 2.2.1), the mass in extinction maps is sometimes increasingly underestimated towards small scales. This biases slopes towards lower values. It is not likely, though, that all features in our extinction maps are massively biased. In particular for Perseus, such would be inconsistent with comparisons between CO and extinction maps (Goodman et al. 2009; also see part I). Still, it is disconcerting that the slope transition does apparently exactly occur in the spatial domain that is not well probed by any tracer.

Interestingly, a cloud-to-core slope transition might not exist in Ophiuchus: note that slopes  $\sim 1$  are observed for radii  $\gtrsim 0.3$  pc, so that no slope transition between cloud and core might be necessary. Specifically, at any given radius, the most massive fragment containing L1688 follows tightly the line connecting the most massive fragments at 0.05 pc and 5 pc radius. If this is true, a clean division between the L1688 dense cores and the surrounding diffuse cloud structure might not exist.

#### 4. INTERPRETATION OF MASS-SIZE DATA

##### 4.1. Larson’s 3<sup>rd</sup> Law and other previous Work

Larson (1981) carried out one of the first studies of mass-size relations of molecular clouds (in his Fig. 5) and obtained  $m(r) \propto r^{1.9}$ . (Actually, he studied size-density relations. Since he assumed spherical cloud geometries, these can be turned into mass-size laws.) Today, this “third Larson law” is usually quoted as  $m(r) \propto r^2$  and considered one of the fundamental properties of cloud structure (e.g., McKee & Ostriker 2007).

We find a nuanced relation between our data and the detailed result of Larson (1981),

$$m(r) = 460 M_{\odot} (r/\text{pc})^{1.9}$$

(our Eq. 1). In the  $1 \leq r/\text{pc} \leq 4$  radius range, his and our results are compatible for several solar neighborhood clouds, as shown by Eq. (7). However, some clouds, like G10, can deviate by about an order of magnitude in mass from this relation. Further, some trends within individual clouds are not described well by one single mass-size law. Slope and intercept of Eq. (6), and the slopes shown in Figs. 4 and 5, may serve as examples for deviant mass-size relations. The Larson (1981) mass-size law thus fails to describe a lot of the cloud substructure visible in state-of-the-art cloud maps. Deviations from this relation have also been noted before (e.g., McKee & Ostriker 2007 for references). Also, note that Larson (1981) never intended to match all cloud substructure; as seen in his Fig. 5, the mass-size relation only provides an order-of-magnitude fit to his data. In this sense, the mass-size laws derived here do not really supersede Larson’s results; molecular clouds are very complex structures, and every one has to be considered individually. However, for certain mass-size trends, Eq. (6) and the global slopes in Fig. 4 do provide a more detailed description than offered by Eq. (1).

Beyond these quantitative differences, Larson’s tech-

nique differs fundamentally from ours. He plotted all cloud and dense core data available to him, and attempted to fit this ensemble data by a common law, independent of whether the cores and clouds were residing in the same area of the sky. Here, however, we usually handle data separately for each cloud, to e.g. calculate the global and tangential slopes shown in Figs. 4 and 5. Only Eqs. (7, 6) stem from an analysis of data combined for several clouds.

Ensemble-based mass-size relations of the kind considered by Larson have been studied by many other groups; here we can only present excerpts from such work. Lada et al. (2008), for example, derive  $b = 2.6$  for dense cores in the Pipe Nebula extinction map used here. For a sample of Infrared Dark Clouds (IRDCs), Ragan et al. (2009) derive even steeper slopes,  $b \approx 3$ , much in excess of any slope derived here. Their approach is very different from ours, though; they extract dense cores, plot their masses and sizes, and fit the data with a single line. We, instead, measure a core’s mass at various contours, and derive tangential slopes by only considering data for a single dense core. Their ensemble slopes thus serve a different purpose than our global and tangential slopes. In this respect, it may be helpful to consider the Type 1–4 linewidth-size relations of Goodman et al. (1998; replace line width with mass in their discussion): there are many different ways to define slopes, and they will characterize different properties. The large-scale structure of molecular clouds, as originally addressed by Larson (1981), is in principle discussed by Solomon et al. (1987) and Heyer et al. (2009). Their data has, however, not been exploited to derive mass-size relations.

Note that Stüwe (1990) uses a technique similar to ours to probe the spatial domain considered here. As discussed in Sec. 4.3, his work is consistent with ours.

#### 4.2. Mass-Size Relations and Star Formation

It is thought since long that clouds need to achieve a high column density in order to produce dense cores and stars. Johnstone et al. (2004), in particular, introduced the concept of extinction (or column density) thresholds for dense core formation (also see: Onishi et al. 1998, Hatchell et al. 2005, Enoch et al. 2007). Similarly, Lombardi et al. (2006) and Lada et al. (2009) argue that a low fraction of mass at high column density yields low star formation activity (also see Kainulainen et al. 2009). This is in line with the Kennicutt-Schmidt law between star formation rate and mass surface density,  $\Sigma_{\text{SFR}} \propto \Sigma_{\text{gas}}^p$  (e.g., Kennicutt 1998). Since  $p \sim 1$  for star-forming clouds (Evans et al. 2009), this relation predicts an increase of star formation activity with increasing column density.

The analysis in Sec. 3 shows that these laws do also manifest in our data. Sections 3.1 and 3.3 suggest that the ability to form clusters and massive stars increases with increasing mass, when considering a given radius. Since  $\langle N_{\text{H}_2} \rangle \propto m/r^2$ , one could also say that cloud fragments do appear to only form massive stars and clusters when they have a high mean column density—just as suggested by the aforementioned laws.

Mass-size studies do, however, also provide information not available from the aforementioned plain column

density studies. First, note that “extinction threshold” studies (e.g., Johnstone et al. 2004) do only consider a single spatial scale, i.e. the beam used to construct the extinction map. This is a major difference to mass-size studies, where many spatial scales are considered. Second, observe that studies of column density distributions (PDFs; e.g., Lombardi et al. 2006) *do* consider all scales of a map, but do not register which part of the signal shown on the histogram originates in which part of the cloud. (Depending on the analysis, this is not necessarily a problem.) Mass-size studies, in contrast, treat individual cloud fragments separately.

Mass-size data sets give a new twist to discussions of extinction thresholds. To see this, consider the solar neighborhood clouds examined here. These are all similar at large spatial scale (Eq. 7). Still, at smaller scale, they differ significantly in mass and star formation activity (Sec. 3.3). The processes determining the star formation activity must thus operate on spatial scales smaller than the entire cloud. In this sense, *the star formation activity depends* (at least in our sample clouds) *on a cloud’s ability to create, from a given mass reservoir, a small number of fragments that dominate the mass reservoir and concentrate it into a small volume.* The presence of high column densities are then a consequence of the cloud structure, but not the governing reason for the formation of dense cores and stars.

#### 4.3. Slopes and Intercepts: Constraints on Density and Physical Cloud Models

The observed power-law-like mass-size relations,

$$m(r) = m_0 (r/\text{pc})^b,$$

are characterized by slopes,  $b$ , and intercepts,  $m_0$ . As we show here, slopes and intercepts can be used to gauge densities and their gradients. At the same time, it is possible to constrain the absolute level of pressure, and the nature of its origin.

Consider, for example, an infinite equilibrium sphere with power-law density profile that is supported by isothermal pressure from gas at temperature  $T_g$ . Then,

$$m(r) = 2.6 M_{\odot} \left( \frac{T_g}{10 \text{ K}} \right) \left( \frac{r}{0.1 \text{ pc}} \right) \quad (8)$$

(Kauffmann et al. 2008, Eq. [13], in their case  $\epsilon \rightarrow \pi/2$ ). Thus, if this model holds, the intercept encodes information on the gas temperature supporting the cloud. Conversely, the slope predicted by the model,  $b = 1$ , can be used to validate the model; if observations yield  $b \neq 1$ , then the model does not apply.

It has to be kept in mind that we consider mass-size laws derived from two-dimensional maps. These are related to, but not identical with, mass-size laws obtained from three-dimensional density maps. This is illustrated by the experiments conducted by Shetty et al. (2010) who use the fragment identification technique also used by us. Their analysis is based on three-dimensional numerical simulations of turbulent clouds. As part of their experiments, they derive mass-size slopes from their data. For their particular set of simulations, the power-law slopes derived in this fashion are similar to the number of dimensions used for mass measurements (i.e., 3 when based on density, and 2 when based on column

density). This underlines that the number of dimensions considered has to be kept in mind.

#### 4.3.1. Density Laws

The above discussion can be extended to include many more models of cloud structure. We do this in two Appendices. The results of this analysis are summarized here.

First, let us examine the connection between mass-size laws and cloud density profiles. Consider a sphere with about constant density for radii smaller than some flattening radius,  $s_0$ , a power-law drop at intermediate radii,  $n(s) \propto s^{-k}$  (where  $s$  is the distance from the center), and vanishing density beyond some outer truncation radius,  $R$ . Such profiles provide a good match to observations of dense cores (Tafalla et al. 2002). They are a good approximation to the structure of isothermal equilibrium spheres (Dapp & Basu 2009). As we show in Appendix A.1, for apertures of radius  $r$ , this yields mass-size relations of the form

$$m(r) \propto n_c r^{3-k} \quad \text{for } s_0 \ll r \ll R, \quad (9)$$

where  $n_c$  is the density for  $s = 0$ , and mass-size slopes

$$d \ln(m)/d \ln(r) = 3 - k \quad \text{for } s_0 \ll r \ll R. \quad (10)$$

Both relations apply only if  $k < 3$ . As the equations show, the intercept contains information on the central density, and the mass-size slope depends on the slope of the density law,  $k$ . Both does, of course, only hold at intermediate radii,  $s_0 \ll r \ll R$ . For reference, we note that the column density obeys  $N \propto r^{1-k}$ .

A generalized version of power-law spheres are tri-axial ellipsoids. Appendix A.3 considers the case in which  $n(s) \propto (s/s_0)^{-k}$  along any main axis, but with  $s_0$  depending on the direction chosen (Eq. A9). Detailed analysis shows that such ellipsoids follow the same mass-size relations as spheres, when  $r = (A/\pi)^{1/2}$ . Thus, the laws listed above apply.

In a next step, one may wish to consider models of cylindrical clouds of length  $\ell$ . Here, we adopt density drops  $n(s) \propto s^{-k}$  perpendicular to the cylinder axis for intermediate values of  $s$ . At intermediate radii  $s_0 \ll r \ll R$ , such clouds obey

$$m(r) \propto n_c r^{4-2k} \quad \Rightarrow \quad d \ln(m)/d \ln(r) = 4 - 2k \quad (11)$$

if their major axis is perpendicular to the line of sight, and

$$m(r) \propto n_c r^{2-k} \quad \Rightarrow \quad d \ln(m)/d \ln(r) = 2 - k, \quad (12)$$

if the axes are aligned. (Intermediate angles are not considered here.) Meaningful relations are only obtained for  $k < 2$ . In both relations, the radius is defined as  $r = (A/\pi)^{1/2}$ .

Thus, just as one may naively expect, the mass-size slope gauges the slope of the density profile. Further, the intercepts of mass-size relations constrain the absolute density of cloud fragments. There is, however, one less obvious fact that calls for attention: the exact relations between mass-size slopes, intercepts, and density law depends on the cloud model and viewing angle. It is therefore not possible to derive the true density profile without further information on the cloud geometry. Such

information may, e.g., be derived by studying the elongation of cloud fragments. Also, the above power-law relations do only apply at intermediate radii,  $s_0 \ll r \ll R$ . This domain might not exist in actual observed clouds. Then, the central density plateau and the finite size have to be considered. These give

$$m(r) \begin{cases} \propto n_c r^2 & \text{for } r \ll s_0 \text{ and} \\ \approx M & \text{for } r \gtrsim R \end{cases} \quad (13)$$

#### 4.3.2. Polytopic Equilibria

The density slopes themselves depend on the processes shaping the model cloud. As a first example, here we consider static equilibrium models in which pressure gradients are in balance with self-gravity. We assume a polytropic equation of state,  $P \propto n^{\gamma_P}$ , in which pressure and density are related by the polytropic exponent,  $\gamma_P$ .

In Appendix B we show that

$$k = \frac{2}{2 - \gamma_P} \quad (14)$$

for polytropic equilibrium spheres (if  $\gamma_P < 4/3$ ) and cylinders (if  $\gamma_P < 1$ ). The density and mass-size slopes are, thus, related to the polytropic exponent. Isothermal pressure, for which  $\gamma_P = 1$ , implies  $k = 2$  in spheres, for example. Then,  $d \ln(m)/d \ln(r) = 1$  in spherical model clouds; laws too complex to be considered here apply to cylinders. As seen in Figs. 4 and 5, such a model can explain some, but not most slope measurements.

Polytropic exponents  $\gamma_P = 1/2$  are sometimes suggested to describe ‘‘turbulent’’ pressure within clouds, as e.g. arising from Alfvén waves (McKee & Zweibel 1995). In this case,  $k = 4/3$ , and so  $d \ln(m)/d \ln(r)$  assumes values of  $5/3 \approx 1.67$  (spheres and ellipsoids),  $4/3 \approx 1.33$  (perpendicularly viewed cylinder), and  $2/3 \approx 0.67$  (end-on cylinder) for the different models. Among these, spheres, ellipsoids, and cylinders viewed from the side provide an acceptable match to the observed mass-size slopes  $b > 1$ . Cylinders viewed along their major axis yield too shallow mass-size laws (and such a viewing direction is highly unlikely).

For a given physical model, the intercept can be used to gauge a cloud’s stability against collapse, respectively suggest the level of supporting pressure. Here, we limit ourselves to the isothermal case, i.e.  $\gamma_P = 1$ . Stability considerations (e.g., of Bonnor-Ebert-type; Ebert 1955, Bonnor 1956) imply

$$M \leq M_{\text{cr}} \approx 2 \frac{\sigma^2(v) R}{G} \quad (15)$$

for the total mass, where  $\sigma(v)$  is the characteristic one-dimensional velocity dispersion (Eqs. B3 and B5). For spheres,  $R$  is the radius, while  $R \rightarrow \ell$  in cylinders. If  $\sigma(v)$  is known (e.g., for thermal pressure),  $M > M_{\text{cr}}$  implies collapse of the object considered. Conversely, depending on the situation,  $\sigma(v)$  can be inferred by requiring that  $M = M_{\text{cr}}$ . Required values of  $\sigma(v)$  significantly in excess of the thermal velocity dispersion of the mean free particle might, e.g., suggest the presence of significant non-thermal pressure. If we only require that pressure balances gravity, and drop the constraint that the object is to be stable against perturbations, the above law yields Eq. (8).

As particular example, consider B68. It is thought that this dense core has a structure very similar to a Bonnor-Ebert sphere (Alves et al. 2001). Thus, one would expect the mass and size of B68 to obey Eq. (8), when considering large enough radii. This is indeed the case, as seen in Fig. 1.

#### 4.4. Synoptic and physical Density Slopes

For intuitive communication, it may be helpful to report synoptic density slopes,

$$\left[ -\frac{d \ln(n)}{d \ln(s)} \right]_{\text{syn}} = 3 - \frac{d \ln(m)}{d \ln(r)}, \quad (16)$$

i.e. the density slope a sphere of the same mass-size slope would have when observed at intermediate radii. The synoptic slopes give a good first idea of the true density slopes. First, recall that the model mass-size laws do not sensitively depend on the assumption of exact spheres; the same relation holds for ellipsoids. Also, in the observed range  $1 \lesssim d \ln(m)/d \ln(r) < 2$ , spheres (or ellipsoids) and perpendicularly viewed cylinders (the end-on view is statistically insignificant) imply similar slopes; for these geometries, the synoptic slopes exceed the true ones by less than 0.5, assuming intermediate radii. Thus, we derive

$$[-d \ln(n)/d \ln(s)]_{\text{syn}} = 1 \text{ to } 2$$

for mass-size slopes  $1 \lesssim d \ln(m)/d \ln(r) < 2$ .

A limited comparison of these density-size slopes with previous results is possible. Tafalla et al. (2002), e.g., study the dust emission of five starless dense cores, and derive density-size slopes of 2.0 to 2.5 for four of them. This is a typical result for cloud fragments of  $\lesssim 0.1$  pc size (Bergin & Tafalla 2007), a spatial domain not too well covered by our data.

Concerning the analysis method and spatial range considered, the extinction study by Stüwe (1990) might provide the best match to our work. Based on star counts, he derives  $-d \ln(n)/d \ln(s) > 1.0 \pm 0.4$  on scales of up to  $\sim 1$  pc. This is consistent with our results, also given the differences in map construction (he uses optical star counts).

## 5. SUMMARY & OUTLOOK

This work studies the internal structure of molecular clouds by breaking individual cloud complexes up into several nested fragments. For these, we derive masses and sizes in order to study their density structure.

Analysis of a limited sample of solar neighborhood cloud complexes (Taurus, Ophiuchus, Perseus, Pipe Nebula, Orion A), as well as more distant clouds (G10 & G11), yields first some basic constraints on mass-size cloud structure. These are as follows.

1. On large spatial scales,  $\geq 1$  pc, the most massive fragments in solar neighborhood clouds—with the possible exception of Orion A—obey

$$m(r) = 400 M_{\odot} (r/\text{pc})^{1.7}$$

(Eq. 7) with deviations  $< 40\%$ . This relation resembles the original mass-size law derived by Larson (1981),  $m(r) = 460 M_{\odot} (r/\text{pc})^{1.9}$ . The

more distant clouds in the sample, however, deviate from this relation by up to an order of magnitude in mass.

2. No single mass-size law can be used to describe all fragments in all clouds. In particular, “Larson’s 3<sup>rd</sup> Law” of constant column density,  $m(r) \propto r^2$ , provides a bad global description; today’s data are too complex to warrant the use of such relations. To give examples, power-law slopes vary with radius within a given cloud (Fig. 5), and clouds can differ massively in mass at given radius (Fig. 2).

In practice, different definitions of mass-size laws are used by different researchers. Also, different definitions may serve different purposes. This must be taken into account when comparing different mass-size laws.

Most importantly, the mass-size data can be used to learn about the formation of stars in molecular clouds. We derive the following constraints.

3. Sample clouds not forming massive stars ( $\gtrsim 10 M_{\odot}$ ) adhere to a limiting mass size relation,

$$m(r) \leq 870 M_{\odot} (r/\text{pc})^{1.33}$$

(Eq. 6), while our sample clouds forming such stars violate this law (Fig. 2). This suggests that the above relation describes the typical mass-size range of molecular clouds not forming high-mass stars. Also, the observations advocate that this boundary constitutes a mass limit for massive star formation. However, such conclusions are based on a small sample and are thus preliminary.

4. Across all clouds studied here, cloud fragments forming clusters are more massive than fragments not doing so (Figs. 1 and 3; Sec. 3.3.1). At given size, cluster-forming fragments dominate the mass reservoir of their host cloud.
5. The mass-size trend of cluster-forming fragments can e.g. be captured by global mass-size slopes (i.e., from 0.05 pc to 5.0 pc radius; Sec. 3.4). Our cluster-forming sample clouds are consistent with a common slope  $\sim 1.27$ . The uncertainties are, unfortunately, significant for a given cloud; slopes may well differ between clouds. In the case of Orion A, e.g., the slope might be as low as  $\sim 0.7$ . However, in any event slopes smaller 1.5 do hold.

Theoretical discussions show that mass-size laws of the form  $m(r) = m_0 (r/\text{pc})^b$  can be related to physical cloud models characterized by power-law density gradients,  $n(s) \propto s^{-k}$ , or polytropic equations of state,  $P \propto n^{\gamma_P}$  (Sec. 4.3). Provided certain idealizations apply,  $b$ ,  $k$ , and  $\gamma_P$  are directly related to another. This analysis suggests the definition of a synoptic density slope,  $[-d \ln(n)/d \ln(s)]_{\text{syn}} = 3 - d \ln(m)/d \ln(r)$  (i.e., assuming the fragment considered was a sphere). This slope provides a first rough estimate of the true density law. Our data gives synoptic density slopes in the range 1 to 2.

We are indebted to a careful and thorough anonymous referee, who saved us from making an embarrassing mis-

take. This project would not have been possible without help from Erik Rosolowsky. His dendrogram analysis code (Rosolowsky et al. 2008) was instrumental for our analysis. Carey et al. (2000), Alves et al. (priv. comm.), Enoch et al. (2006), Lombardi et al. (2006), Ridge et al. (2006), Román-Zúñiga et al. (2009), and Thompson et

al. (in prep.) contributed maps to the present study. We are grateful for their help. This work was in part made possible through Harvard Interfaculty Initiative funding to the Harvard Initiative in Innovative Computing (IIC). It is based upon work supported by the National Science Foundation under Grant No. AST-0908159.

## REFERENCES

- Alves, J., Lada, C., & Lada, E. 2001, *Nature*, 409, 159  
 Ballesteros-Paredes, J., Klessen, R., Mac Low, M.-M., & Vazquez-Semadeni, E. 2007, in *Protostars and Planets V*, ed. B. Reipurth, D. Jewitt, & K. Keil, 63–80  
 Bally, J., Lanber, W., Stark, A., & Wilson, R. 1987, *ApJ*, 312, L45  
 Bergin, E., & Tafalla, M. 2007, *ARA&A*, 45, 339  
 Beuther, H., Churchwell, E. B., McKee, C. F., & Tan, J. C. 2007, in *Protostars and Planets V*, ed. K. K. B. Reipurth D. Jewitt, 165–180  
 Bonnor, W. 1956, *MNRAS*, 116, 351  
 Brooke, T. Y., Huard, T. L., Bourke, T. L., Boogert, A. C. A., Allen, L. E., Blake, G. A., Evans, Neal J., I., Harvey, P. M., Koerner, D. W., Mundy, L. G., Myers, P. C., Padgett, D. L., Sargent, A. I., Stapelfeldt, K. R., van Dishoeck, E. F., Chapman, N., Cieza, L., Dunham, M. M., Lai, S.-P., Porras, A., Spiesman, W., Teuben, P. J., Young, C. H., Wahhaj, Z., & Lee, C. W. 2007, *The Astrophysical Journal*, 655, 364  
 Cambrésy, L. 1999, *A&A*, 345, 965  
 Carey, S. J., Feldman, P. A., Redman, R. O., Egan, M. P., MacLeod, J. M., & Price, S. D. 2000, *The Astrophysical Journal*, 543, L157  
 Curry, C., & McKee, C. 2000, *ApJ*, 528, 734  
 Dapp, W., & Basu, S. 2009, *MNRAS*, 395, 1092  
 Ebert, R. 1955, *Zeitschrift für Astrophysics*, 37, 217  
 Enoch, M., Glenn, J., Evans II, N., Sargent, A., Young, K., & Huard, T. 2007, *ApJ*, 666, 982  
 Enoch, M., Young, K., Glenn, J., Evans II, N., Golwala, S., Sargent, A., Harvey, P., Aguirre, J., Goldin, A., Haig, D., Huard, T., Lange, A., Laurent, G., Maloney, P., Mouskops, P., Rossinot, P., & Sayers, J. 2006, *ApJ*, 638, 293  
 Evans, N. J., Dunham, M. M., Jørgensen, J. K., Enoch, M. L., Merín, B., van Dishoeck, E. F., Alcalá, J. M., Myers, P. C., Stapelfeldt, K. R., Huard, T. L., Allen, L. E., Harvey, P. M., van Kempen, T., Blake, G. A., Koerner, D. W., Mundy, L. G., Padgett, D. L., & Sargent, A. I. 2009, *ApJS*, 181, 321  
 Forbrich, J., Lada, C. J., Muench, A. A., Alves, J., & Lombardi, M. 2009, *ApJ*, 704, 292  
 Goodman, A., Barranco, J., Wilner, D., & Heyer, M. 1998, *ApJ*, 504, 223  
 Goodman, A. A., Pineda, J. E., & Schnee, S. L. 2009, *ApJ*, 692, 91  
 Gutermuth, R. A., Megeath, S. T., Myers, P. C., Allen, L. E., Pipher, J. L., & Fazio, G. G. 2009, *The Astrophysical Journal Supplement Series*, 184, 18  
 Hatchell, J., Richer, J., Fuller, G., Quattrone, C., Ladd, E., & Chandler, C. 2005, *A&A*, 440, 151  
 Heyer, M., Krawczyk, C., Duval, J., & Jackson, J. 2009, *ApJ*, 699, 1092  
 Horedt, G. 1987, *Ap&SS*, 133, 81  
 Johnstone, D., Di Francesco, J., & Kirk, H. 2004, *ApJ*, 611, L45  
 Johnstone, D., Wilson, C., Moriarty-Schieven, G., Joncas, G., Smith, G., Gregersen, E., & Fich, M. 2000, *ApJ*, 545, 327  
 Kainulainen, J., Beuther, H., Henning, T., & Plume, R. 2009, *Astronomy and Astrophysics*, 508, L35  
 Kauffmann, J., Bertoldi, F., Bourke, T., Evans II, N., & Lee, C. 2008, *A&A*, 487, 993  
 Kauffmann, J., Pillai, T., Shetty, R., Myers, P. C., & Goodman, A. A. 2010, *The Astrophysical Journal*, 712, 1137  
 Kennicutt, R. C. 1998, *ApJ*, 498, 541  
 Kenyon, S., Gómez, M., & Whitney, B. 2008, *Low Mass Star Formation in the Taurus-Auriga Clouds*, ed. B. Reipurth, 405–+  
 Kirk, H., Johnstone, D., & Di Francesco, J. 2006, *ApJ*, 646, 1009  
 Lada, C., Muench, A., Rathborne, J., Alves, J., & Lombardi, M. 2008, *ApJ*, 672, 410  
 Lada, C. J., Lombardi, M., & Alves, J. F. 2009, *ApJ*, 703, 52  
 Larson, R. 1981, *MNRAS*, 194, 809  
 Lombardi, M., Alves, J., & Lada, C. 2006, *A&A*, 454, 781  
 Lombardi, M., Lada, C., & Alves, J. 2008, *A&A*, 489, 143  
 McKee, C., & Holliman, J. 1999, *ApJ*, 522, 313  
 McKee, C., & Ostriker, E. 2007, *ARA&A*, 45, 565  
 McKee, C., & Zweibel, E. 1995, *ApJ*, 440, 686  
 Menten, K. M., Pillai, T., & Wyrowski, F. 2005, in *IAU Symposium, Vol. 227, Massive Star Birth: A Crossroads of Astrophysics*, ed. E. C. M. W. R. Cesaroni M. Felli, 23–34  
 Motte, F., Andre, P., & Neri, R. 1998, *A&A*, 336, 150  
 Nutter, D., & Ward-Thompson, D. 2007, *MNRAS*, 374, 1413  
 Onishi, T., Mizuno, A., Kawamura, A., Ogawa, H., & Fukui, Y. 1998, *ApJ*, 502, 296  
 Ostriker, J. 1964, *ApJ*, 140, 1056  
 Peretto, N., & Fuller, G. A. 2009, *Astronomy and Astrophysics*, 505, 405  
 Pillai, T., Wyrowski, F., Carey, S. J., & Menten, K. M. 2006a, *Astronomy and Astrophysics*, 450, 569  
 Pillai, T., Wyrowski, F., Hatchell, J., Gibb, A. G., & Thompson, M. A. 2007, *A&A*, 467, 207  
 Pillai, T., Wyrowski, F., Menten, K., & Krügel, E. 2006b, *A&A*, 447, 929  
 Ragan, S., Bergin, E., & Gutermuth, R. 2009, *ApJ*, 698, 324  
 Ridge, N., Di Francesco, J., Kirk, H., Li, D., Goodman, A., Alves, J., Arce, H., Borkin, M., Caselli, P., Foster, J., Heyer, M., Johnstone, D., Kosslyn, D., Lombardi, M., Pineda, J., Schnee, S., & Tafalla, M. 2006, *AJ*, 131, 2921  
 Román-Zúñiga, C. G., Lada, C. J., & Alves, J. a. F. 2009, *The Astrophysical Journal*, 704, 183  
 Rosolowsky, E., Pineda, J., Kauffmann, J., & Goodman, A. 2008, *ApJ*, 679, 1338  
 Rowles, J., & Froebrich, D. 2009, *MNRAS*, 395, 1640  
 Shetty, R., Collins, D. C., Kauffmann, J., Goodman, A. A., Rosolowsky, E. W., & Norman, M. L. 2010, *The Astrophysical Journal*, 712, 1049  
 Solomon, P., Rivolo, A., Barrett, J., & Yahil, A. 1987, *ApJ*, 319, 730  
 Stüwe, J. A. 1990, *A&A*, 237, 178  
 Tafalla, M., Myers, P., Caselli, P., Walmsley, C., & Comito, C. 2002, *ApJ*, 569, 815  
 Thompson, M. A., Hatchell, J., Walsh, A. J., MacDonald, G. H., & Millar, T. J. 2006, *A&A*, 453, 1003  
 Viala, Y., & Horedt, G. 1974, *A&A*, 33, 195  
 Williams, J., Blitz, L., & McKee, C. 2000, *Protostars and Planets IV*, 97  
 Williams, J., de Geus, E., & Blitz, L. 1994, *ApJ*, 428, 693  
 Wood, D. O. S., & Churchwell, E. 1989, *ApJS*, 69, 831

## APPENDIX

## A. MODEL MASS-SIZE RELATIONS

Here we consider density profiles of the form

$$n(s) \propto s^{-k} \quad (\text{A1})$$

in the domain  $s_0 \ll s \ll R$ . In spheres,  $s$  is the distance from the density peak, while it is the distance from the main axis in cylinders. Densities become about constant for  $s \lesssim s_0$ , and they vanish for  $s > R$ .

### A.1. Spheres at Intermediate Radii

Integration along the line of sight gives the column density at offset  $u$ ,

$$N(u) = 2 \int_0^{[R^2 - u^2]^{1/2}} n([u^2 + w^2]^{1/2}) dw, \quad (\text{A2})$$

where the integration stops at the boundary radius. Evaluation yields

$$N(u) \propto u^{1-k} \quad (R \rightarrow \infty) \quad (\text{A3})$$

if  $k > 1$ , a relation that can be used for offsets  $s_0 \ll u \ll R$ . Integration of the column density over a circular peak-centered aperture of maximum offset  $u$  gives the mass,

$$m(u) = 2\pi\mathcal{C} \int_0^u N(w) w dw, \quad (\text{A4})$$

where  $\mathcal{C} = \Sigma/N_{\text{H}_2} = \mu_{\text{H}_2} m_{\text{H}}$  is the conversion factor to mass surface density. Evaluation in the limit  $R \rightarrow \infty$  gives

$$m(u) \propto u^{3-k} \quad \Rightarrow \quad m(r) \propto r^{3-k} \quad (\text{A5})$$

for  $s_0 \ll r \ll R$ . We use  $u = r$  in the transition from offsets to aperture sizes since, in spheres, the offset from the center,  $u$ , is equal to the radius defined via the aperture area,  $r = (A/\pi)^{1/2}$ .

The meaningful range of this relation is limited to  $k < 3$ ; for  $k \geq 3$ , the mass would decrease with size, which is not physical. In essence, spheres with  $k \geq 3$  have a finite mass, even for  $R \rightarrow \infty$ , so that power-law mass-size relations cannot hold in any radius domain.

### A.2. Homogeneous Spheres

Homogeneous spheres, in which the density is spatially constant, constitute a special case of the aforementioned spherical models. Consider an offset  $u$  from the sphere's center, where the density drops to zero beyond the sphere's outer radius,  $R$ . Then, the column density is the product of the density,  $n_0$ , and the length of the line of sight,

$$N(u) = 2n_0(R^2 - u^2)^{1/2}. \quad (\text{A6})$$

Integration following Eq. (A4) yields (with the substitution  $u \rightarrow r$ )

$$m(r) = \frac{4}{3}\pi\varrho_0 \left[ R^3 - (R^2 - r^2)^{3/2} \right], \quad (\text{A7})$$

in which  $\varrho_0 = \mathcal{C}n_0$  is the mass density corresponding to  $n_0$ . For  $r \rightarrow R$  we derive  $m = 4/3\pi\varrho_0 R^3$ , just as expected for a homogeneous sphere truncated at radius  $R$ . The slope obeys

$$\frac{d \ln(m)}{d \ln(r)} = 3 \frac{(R^2 - r^2)^{1/2} r^2}{R^3 - (R^2 - r^2)^{3/2}} \quad (\text{A8})$$

and does monotonously decrease from  $d \ln(m)/d \ln(r) = 2$  at  $r = 0$  to  $d \ln(m)/d \ln(r) = 0$  at  $r = R$ .

### A.3. Triaxial Ellipsoids at Intermediate Radii

Another variation of spherical power-law density profiles are triaxial density distributions with ellipsoidal iso-density surfaces. These can be derived from spherical power-laws by substituting  $s/s_0 \rightarrow [(x/x_0)^2 + (y/y_0)^2 + (z/z_0)^2]^{1/2}$  (where a subscript '0' indicates reference properties for normalization). The coordinates  $x$ ,  $y$ , and  $z$  give the projection of a given position on the three axes of the ellipsoidal density distribution. Then, the density law reads

$$n = n_0 \left[ \left( \frac{x}{x_0} \right)^2 + \left( \frac{y}{y_0} \right)^2 + \left( \frac{z}{z_0} \right)^2 \right]^{-k/2}. \quad (\text{A9})$$

The chosen coordinates form an orthogonal coordinate system. Any position along a straight line of sight,  $w$ , is therefore linearly related to the coordinates chosen for the density distribution:

$$x = m_x + n_x w; \quad y = m_y + n_y w; \quad z = m_z + n_z w. \quad (\text{A10})$$

For convenience, here we choose that  $w = 0$  at the position of highest density along the line of sight. Substitution of Eqs. (A10) into Eq. (A9) yields

$$n = n_0 \left[ \frac{m_x^2}{x_0^2} + \frac{m_y^2}{y_0^2} + \frac{m_z^2}{z_0^2} + 2 \left( \frac{m_x n_x}{x_0} + \frac{m_y n_y}{y_0} + \frac{m_z n_z}{z_0} \right) w + \left( \frac{n_x^2}{x_0^2} + \frac{n_y^2}{y_0^2} + \frac{n_z^2}{z_0^2} \right) w^2 \right]^{-k/2}, \quad (\text{A11})$$

i.e., some terms that do not contain  $w$ , some that include  $w$  linearly, and a few that contain  $w$  to its square. Analysis shows that the sum of the terms with a linear dependence on  $w$  must be zero. To see this, consider the requirement that the density reaches its maximum where  $w = 0$ . For this to happen, the derivative of the sum within the square brackets of Eq. A11 with respect to  $w$  must vanish at  $w = 0$ . This is only the case if all terms linear in  $w$  cancel out. Equation (A11) can thus be written

$$n = n_0 \left( \frac{u^2 + w^2}{r_0} \right)^{-k/2}, \quad (\text{A12})$$

if one chooses  $u^2 = (m_x^2/x_0^2 + m_y^2/y_0^2 + m_z^2/z_0^2) \cdot (n_x^2/x_0^2 + n_y^2/y_0^2 + n_z^2/z_0^2)^{-1}$  and  $r_0^2 = (n_x^2/x_0^2 + n_y^2/y_0^2 + n_z^2/z_0^2)^{-1}$ . Formally, Eq. (A12) is identical to the spherical density law substituted in Eq. (A2). Therefore, we can use the calculations in Appendix A.1 to conclude that, again,

$$N(u) \propto u^{1-k} \quad (R \rightarrow \infty) \quad (\text{A13})$$

if  $k > 1$ . Thus, the spatial column density distribution does only depend on  $u$ .

A detailed look at the above analysis does actually show that we did not use the exact nature of the density law to this point. Instead, we exploited that the density depends on  $(x/x_0)^2 + (y/y_0)^2 + (z/z_0)^2$ . Thus, we can make the conclusion that *all* density distributions with ellipsoidal iso-density surfaces yield column density distributions only depending on  $u$ .

Thus,  $u$  can be interpreted as an offset, just as in the spherical situation. Inspection of the equation defining  $u$  reveals that the three-dimensional offsets from the distribution's center,  $m_i$ , form a triaxial ellipsoid too, when  $u$  is kept constant. Projection of the  $u = \text{const.}$  surface into a plane corresponds to a cut through this ellipsoid. Since cuts through ellipsoids yield ellipses, the  $u = \text{const.}$  curve in a plane is an ellipse too. In this case, spatial integration of the column density can be conveniently executed in polar coordinates. Let  $v$  and  $w$  be the minor and major axis of the projected ellipse. For a given viewing perspective,  $v/w$  is constant for all contours of constant column density. Then, the mass follows from

$$m(u) = 2\pi (v/w) \mathcal{C} \int_0^u N(w) w \, dw, \quad (\text{A14})$$

where we use that the ellipse's area increases with  $w$  as  $2\pi (v/w) w \, dw$ . This integral becomes

$$m(u) \propto u^{3-k} \quad \Rightarrow \quad m(r) \propto r^{3-k} \quad (\text{A15})$$

for  $s_0 \ll r \ll R$ . In this, we use that  $u$  is proportional to the effective radius of the ellipsoid formed by  $N = \text{const.}$  (i.e.,  $u = \text{const.}$ ) contours. The latter holds since, for a given ellipsoid,  $v/w$  is a constant, and its area is  $\pi v w = \pi (v/w) w^2$ . Thus, the effective radius becomes  $r = (v/w)^{1/2} w \propto w$ .

In summary, we retrieve the relations already derived for spheres, including the limits on reasonable values of  $k$ . As expected, spheres form a particular case of ellipsoids with  $x_0 = y_0 = z_0$ .

#### A.4. Cylinders at Intermediate Radii: Perpendicular View

In cylinders with the main axis perpendicular to the line of sight, the integration in Eq. (A2) must be evaluated with the integration path perpendicular to the cylinder axis. Then

$$N(u) \propto u^{1-k} \quad (R \rightarrow \infty), \quad (\text{A16})$$

as long as  $k > 1$ . This provides, again, a convenient description for  $s_0 \ll u \ll R$ . Since the column density is constant for given offset,  $u$ , apertures along a given column density contour have a size  $2u\ell$ , where  $\ell$  is the cylinder length. Such an aperture contains a mass

$$m(u) = 2\ell \mathcal{C} \int_0^u N(w) \, dw. \quad (\text{A17})$$

Substitution yields

$$m(u) \propto u^{2-k} \quad \Rightarrow \quad m(r) \propto r^{4-2k}. \quad (\text{A18})$$

This relation is applicable if  $k < 2$ , following the discussion of finite masses for spheres. In the transition from  $u$  to  $r$  we use that  $r = (2\ell u/\pi)^{1/2}$ , which gives  $u \propto r^2$ .

#### A.5. Cylinders at Intermediate Radii: Parallel View

In cylinders with the main axis aligned with the line of sight, the integration in Eq. (A2) must be evaluated along the cylinder axis. In this case,

$$N(u) = n(u) \cdot \ell. \quad (\text{A19})$$

This geometry further implies

$$m(u) = 2\pi \mathcal{C} \int_0^u N(w) w \, dw, \quad (\text{A20})$$

which gives

$$m(u) \propto u^{2-k} \quad \Rightarrow \quad m(r) \propto r^{2-k} \quad (\text{A21})$$

in the usual  $s_0 \ll u \ll R$  limit, with the further constrain that  $k < 2$ . As in spheres,  $u = r$  for contours of constant column density.

#### A.6. Very large and small Radii

For central flattening of the density profile, the column density becomes constant for  $u \ll s_0$ , independent of the model adopted. Then, the mass in a given aperture is just given by the product of the mass surface density, which scales with  $n_c R$ , and the aperture area. For large radii, the mass is equal to the total mass when considering apertures larger than the object's size. Thus

$$m(r) \begin{cases} \propto n_c R r^2 & \text{for } r \ll s_0, \text{ and} \\ \approx M & \text{for } r \gtrsim R, \end{cases} \quad (\text{A22})$$

independent of the adopted model geometry.

### B. POLYTROPIC EQUILIBRIUM CLOUD MODELS

Polytropic cloud models assume an equation of state of the form

$$P = P_0 (\rho/\rho_0)^{\gamma_P}. \quad (\text{B1})$$

They are in particular used to solve the equation of hydrostatic equilibrium,  $\vec{\nabla}P = -\rho \vec{\nabla}\Phi$ , where the gravitational potential fulfills the Poisson equation,  $\vec{\nabla}^2\Phi = 4\pi G\rho$ .

#### B.1. Polytropic Equilibrium Spheres

Hydrostatic equilibrium spheres supported by polytropic pressure have recently been summarized by McKee & Holliman (1999) and Curry & McKee (2000). In spherical symmetry,  $\vec{\nabla} \rightarrow \partial/\partial s$ ,  $\Phi(s) = -Gm(s)/s$ , and  $m(s) = 4\pi \int_0^s \rho(w) w dw$ . This differential equation can easily be solved for density profiles  $\rho(s) \propto s^{-k}$ . Solutions are, however, only physical for  $k < 3$ ; the power-law implies  $m(s) \propto s^{3-k}$ , which only increases with radius if  $k$  is small enough. The hydrostatic equation implies  $s^{-\gamma_P k - 1} \propto s^{1-2k}$ . This can only be fulfilled if both exponents to  $s$  are identical, which implies

$$k = \frac{2}{2 - \gamma_P} \quad (\gamma_P < 4/3), \quad (\text{B2})$$

where the limit on  $\gamma_P$  reflects the condition  $k < 3$ . Stability against perturbations implies that the mass of the equilibrium is smaller than some critical mass (McKee & Holliman 1999). For  $\gamma_P = 1$ , this critical mass is identical to the Bonnor-Ebert mass,

$$M_{\text{cr}} = 2.4 \frac{\sigma^2(v) R}{G}, \quad (\text{B3})$$

where the numerical constant follows the discussion by McKee & Holliman (1999). Stable clouds have  $M < M_{\text{cr}}$ .

#### B.2. Polytropic Equilibrium Cylinders

Horedt (1987) presents a summary of hydrostatic equilibrium cylinders (as well as sheets and spheres) supported by polytropic pressure. It builds on discussions of the case  $\gamma_P \geq 1$  by Ostriker (1964), and analysis of polytropes with  $\gamma_P < 1$  by Viala & Horedt (1974).

The Poisson equation can be tackled using the divergence theorem,  $\int_V \vec{\nabla} \cdot \vec{F} dV = \int_{\partial V} \vec{F} \cdot d\vec{A}$ . When analyzing this equation for the volume of an infinitely long cylinder, the ends can be neglected in the integration over the volume's surface,  $\partial V$ . Thus, if the component of  $\vec{F}$  perpendicular to the cylinder surface is constant, and assumes the value  $F_{\perp}$  along it, then  $|\int_{\partial V} \vec{F} \cdot d\vec{A}| = 2\pi \ell s F_{\perp}$  for cylinders of length  $\ell$  and radius  $s$ . To apply this analysis to the Poisson equation, we substitute  $\vec{F} \rightarrow \vec{\nabla}\Phi$ . In cylindric coordinates, the component of the potential's gradient that is perpendicular to the cylinder surface implies the substitution  $F_{\perp} \rightarrow \partial\Phi/\partial s$ . In essence, combination of the Poisson equation and the divergence theorem yields  $4\pi G \int_V \rho dV = \int_{\partial V} \partial\Phi/\partial s dA$ , which evaluates to  $\partial\Phi/\partial s = 2Gm(s)/(s\ell)$ , where  $m(s)$  is the mass within the radius  $s$ . For  $\ell \rightarrow \infty$ , we further have  $\vec{\nabla} \rightarrow \partial/\partial s$ , and so the hydrostatic equation becomes  $\partial P/\partial s = -\rho \partial\Phi/\partial s$ .

A simple solution is provided by  $\rho(s) \propto s^{-k}$ , which implies  $s^{-\gamma_P k - 1} \propto s^{1-2k}$ , just as found for the spherical case. Analysis of the integral for the mass implies  $k < 2$ , similar to what is found for spheres. Thus, solutions must fulfill

$$k = \frac{2}{2 - \gamma_P} \quad (\gamma_P < 1), \quad (\text{B4})$$

where the limit enforces  $k < 2$ . A perturbation analysis analog to the spherical Bonnor-Ebert case gives a critical limiting mass

$$M_{\text{cr}} = 2 \frac{\sigma^2(v) \ell}{G} \quad (\text{B5})$$

for  $\gamma_P = 1$ , as e.g. demonstrated by Ostriker (1964).